Comput Mech (2008) 43:151–159
DOI 10.1007/s00466-008-0325-8

ORIGINAL PAPER

Fluid–structure interaction modeling of a patient-specific cerebral aneurysm: influence of structural modeling

Ryo Torii · Marie Oshima · Toshio Kobayashi · Kiyoshi Takagi · Tayfun E. Tezduyar

Received: 21 April 2008 / Accepted: 22 July 2008 / Published online: 10 September 2008

Abstract Fluid–structure interaction (FSI) simulations of a cerebral aneurysm with the linearly elastic and hyper-elastic wall constitutive models are carried out to investigate the influence of the wall-structure model on patient-specific FSI simulations. The maximum displacement computed with the hyper-elastic model is 36% smaller compared to the linearly elastic material model, but the displacement patterns such as the site of local maxima are not sensitive to the wall models. The blood near the apex of an aneurysm is likely to be stagnant, which causes very low wall shear stress and is a factor in rupture by degrading the aneurysmal wall. In this study, however, relatively high flow velocities due to the interaction between the blood flow and aneurysmal wall are seen to be independent of the wall model. The present results indicate that both linearly elastic and hyper-elastic models can be useful to investigate aneurysm FSI.

R. Torii (✉)
Department of Chemical Engineering, Imperial College,
South Kensington Campus, London SW7 2AZ, UK
e-mail: r.torii@imperial.ac.uk

M. Oshima · K. Takagi
Institute of Industrial Science, The University of Tokyo,
4-6-1 Komaba, Meguro, Tokyo 153-8505, Japan

T. Kobayashi
Japan Automobile Research Institute,
2530 Karima, Tsukuba, Ibaraki 305-0822, Japan

K. Takagi
Department of Neurosurgery, Fujita Health University,
1-98 Dengakugakubo, Kutsukake, Toyoake, Aichi 470-1192, Japan

T. E. Tezduyar
Mechanical Engineering, Rice University, MS 321,
6100 Main Street, Houston, TX 77005, USA

Keywords Fluid–structure interaction · Cerebral aneurysm · Patient-specific modeling · Structural model

1 Introduction

Because hemodynamic forces such as blood pressure and wall shear stress (WSS) play a significant role in initiation, growth and rupture of cerebral aneurysm [1], predicting those forces on the aneurysmal wall can help with estimating the risk factors for aneurysm. We have been investigating the WSS distribution near the aneurysmal site with fluid–structure interaction (FSI) computations to better understand the role of hemodynamics in aneurysm. In particular, we reported earlier that the WSS on and mechanical stress in the aneurysmal walls are significantly increased by hypertensive blood pressure [2], which is known as a risk factor in rupture of aneurysms causing subarachnoid hemorrhage [3,4].

For aneurysms at the middle cerebral artery bifurcation, the WSS patterns are determined by the nature of the flow entering the aneurysm or impinging on the arterial wall near the aneurysm, in conjunction with the wall deformation. The wall deformation, governed by the linear momentum balance equations of the the arterial wall, can be influenced by the structural model used for the arterial wall as well as by the nature of the aneurysm geometry [5]. Structural modeling of the arterial wall has been a widely discussed issue in cardiovascular biomechanics [6,7]. The simplest way to model the arterial wall is to assume it to be made of linearly elastic material. The biggest advantage of this approach is the low computational cost. And the pressure–radius relationship of a straight arterial segment modeled with the linearly elastic wall model sufficiently agrees with the experimental data within the physiological pressure range [8]. This approach is adopted even these days; e.g. the small-on-large concept

proposed by Baek and co-workers [9] is based on linearly elastic behavior of the arterial wall deformation in the physiological pressure range, and it is particularly successful in large-scale patient-specific FSI computations [10]. Hyper-elastic material model is also widely used in arterial wall mechanics simulations [11,12] and cardiovascular FSI computations [13–16]. This approach enables the modeling of the incompressibility and stiffening behavior of the arterial wall under high strain. The number of model parameters is generally not too many and the computational cost is affordable. More sophisticated wall models have also been developed, with the viscoelastic, unisotropic and inhomogeneous characteristics of the arterial wall, owing to collagen fiber and other multiple compositions [17,18], and adopted in arterial wall mechanics problems. Using such sophisticated material models is desirable, especially because in a diseased artery the compositions are more diverse and complicated [19]. However, application of these material models to patient-specific geometries is still scarce [20] because patient-specific information on the arterial composition, such as the fiber orientation, sites of lipid accumulation and calcification and their material properties, are very difficult to obtain in vivo. Hence in patient-specific cardiovascular simulations, arterial wall is still modeled with linearly elastic or hyper-elastic material models. In this paper, influence of the structural model on patient-specific FSI computations is examined because the number of studies on the influence of the wall model in patient-specific simulation, particularly in terms of FSI, is still limited [15,16,21]. FSI simulations of a patient-specific cerebral aneurysm with linearly elastic and hyper-elastic constitutive models are carried out and the results are compared.

2 Computational method

2.1 FSI modeling

The 3D Navier–Stokes equations of incompressible flow are solved to compute the blood flow. The blood flow in the cerebral arteries is assumed to be laminar [22]. The fluid mechanics with deforming walls is computed with the Deforming-Spatial-Domain/Stabilized Space–Time (DSD/SST) method [23–26], with the streamline-upwind /Petrov-Galerkin (SUPG) [27,28] and pressure-stabilizing/Petrov-Galerkin (PSPG) [23,29] formulations for stabilization. An earlier version of the pressure stabilization, for Stokes flows, was introduced in [30]. The DSD/SST method was introduced for flows with moving boundaries and interfaces and has been applied to a large class of problems [31–38], including FSI [39–45]. New versions of the DSD/SST method were introduced in [45] together with new versions of the space–time FSI technique.

The structural mechanics, governed by the linear momentum balance equations, is computed with the Galerkin finite element method. The arterial structure in this study is modeled in three different ways: (1) linearly elastic material with small-strain assumption (LESS), (2) linearly elastic material with finite strain (LEFS), and (3) hyper-elastic (HE) material (with finite strain). The weak form of the governing equation is

$$\int_{\Omega_0} \mathbf{w} \cdot \frac{\partial^2 \mathbf{x}}{\partial t^2} d\Omega + \int_{\Omega_0} \delta \mathsf{E} : \mathsf{S} d\Omega = \int_{\Gamma_t} \mathbf{w} \cdot \mathbf{t} d\Gamma + \int_{\Omega_t} \mathbf{w} \cdot \rho \mathbf{f} d\Omega, \tag{1}$$

where $\mathbf{x}$ is the displacement vector, $\mathbf{t}$ is the traction vector at the boundary, ρ is the density of arterial wall, $\mathbf{f}$ is the body force vector, and $\mathbf{w}$ is the test function, which is also the virtual displacement. The symbols E and S denote the Green–Lagrange strain tensor and Second Piola–Kirchhoff stress tensor, respectively. For the model under small strain assumption, the stress is evaluated with the Cauchy stress tensor. For the hyper-elastic material model, the second Piola–Kirchhoff stress tensor S is defined as

$$\mathsf{S} = 2\frac{\partial W}{\partial \mathsf{C}}, \tag{2}$$

where W is the strain energy function and C is the right Cauchy–Green deformation tensor. The incompressibility constraint is enforced with a mixed displacement/pressure method using a Lagrange multiplier λ as follows:

$$\mathsf{S} = 2\left(\frac{\partial W}{\partial \mathsf{C}} + \lambda \frac{\partial}{\partial \mathsf{C}}(I_3 - 1)\right), \tag{3}$$

where I_3 is the third invariant of C. The Lagrange multiplier is linked to the hydrostatic pressure as $\lambda = -p/2$ [46]. The Fung material model, with the strain-energy function

$$W = \frac{a}{b}\left[\exp\left(\frac{b}{2}(I_1 - 3)\right) - 1\right], \tag{4}$$

is adopted in this study based on the experimental work of Delfino and co-workers [47]. Here I_1 is the first invariant of C.

The fluid and structural mechanics systems are coupled at the interface by the kinematic and dynamic conditions, and are solved with a block-iterative coupling approach [43,48]. The fluid mesh is updated by using an automatic mesh moving method [31,49], where the motion of the nodal points is governed by the equations of elasticity. The computational method is described in more detail in [50].

2.2 Modeling aneurysm geometry and mechanical properties

An aneurysm model at the middle cerebral artery (MCA) bifurcation was reconstructed based on CT images using the marching-cubes method. The subject was a 67-year-old female; the aneurysm was unruptured when it was scanned.

Approximately 150 CT slices with 0.60 mm interval were used for the geometry reconstruction. Each slice consists of 512 × 512 pixels. The in-plane resolution of a slice is 0.3125 mm/pixel. The reconstruction was carried out with the commercial software ALATOVIEW (Toshiba medical, Inc.). Because the arterial wall was not thick enough to be resolved in the CT images, it was added by assuming a uniform wall thickness of 0.3 mm and inflating the lumenal wall outward. The diameter of the arterial lumen at the inlet is 2.38 mm and the diameters at the two distal ends are 1.51 and 2.01 mm.

The blood is assumed to be Newtonian in this study because the apparent viscosity of blood is known to be nearly constant when the shear rates are high [51]. The density and kinematic viscosity of the blood are set to 1,000 kg/m^3 and 4.0×10^{-6} m^2/s, respectively. The density, elastic modulus and Poisson's ratio for the linearly elastic arterial wall models are set to 1,000 kg/m^3, 1.0 MPa and 0.49. For the hyper-elastic arterial model, the parameters a and b in Eq. (4) are determined based on experimental observations with a porcine carotid artery and set to 353.6 kPa and 16.7, respectively [47]. The parameters were recalculated to obtain the pressure-radius correlation within physiological pressure range, 80–120 mm Hg, by comparing computationally obtained pressure-radius relationship with an experimental results [52]. Hence the influence of residual stress is somewhat taken into account in this study.

Eight-noded hexahedral elements are used for the finite element discretization as shown in Fig. 1. First-order interpolation functions are employed for all variables apart from the hydrostatic pressure in the arterial wall model, which is interpolated with piecewise-constant functions. The number of nodes and elements are 53,769 and 50,240 for the fluid mechanics part and 17,397 and 11,480 for the structural mechanics part. The wall thickness is resolved with two layers of elements.

2.3 Boundary conditions

The inflow boundary conditions are represented by a pulsatile velocity profile prescribed by Womersley's formulation [53] based on a waveform from ultrasound Doppler velocimeter at the carotid artery of a healthy male volunteer in his 20's. The inflow waveform is shown in Fig. 2 with the flow waveform calculated based on the original velocity recording. For realistic FSI computations, it is essential to apply the

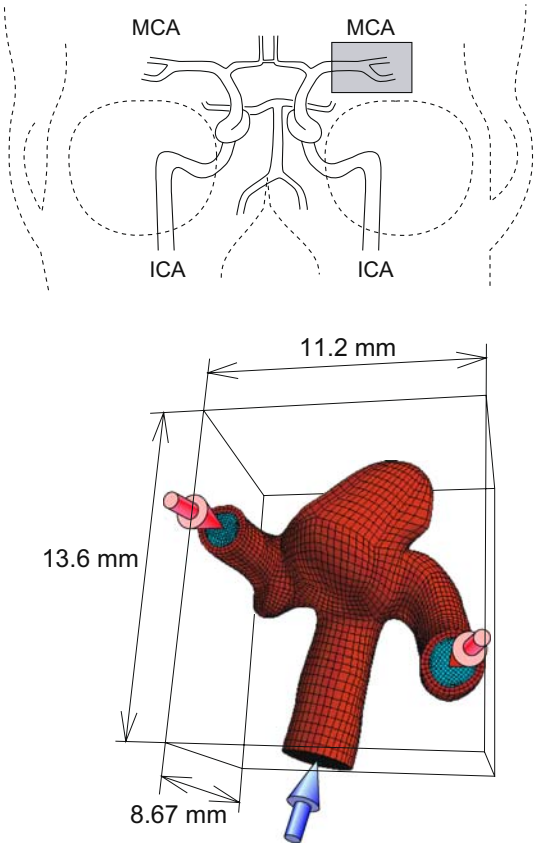

Fig. 1 Computational model of a middle cerebral arterial aneurysm. The middle cerebral artery (MCA) in the intracranial arterial tree (*top*) and the mesh (*bottom*). The *blue arrow* indicates the inlet and the *red arrows* indicate the outlets

physiological pressure conditions as well as the velocity conditions to simulate deformation of the arterial wall. The pressure conditions in our study are modeled by the normal stress at the boundaries, which are shown with red arrows in Fig. 1. The time-dependent pressure is obtained by

$$P = P_0 + QR, \tag{5}$$

where Q is the total outflow (=inflow). Here P_0 is a reference pressure and R represents the resistance due to the distal vascular tree, and they were determined to obtain the physiological pressure range 80–120 mm Hg (10,640–15,960 Pa). The pressure waveform is shown in Fig. 2. The pressure waveform is assumed to vary in phase with the inflow. At the interface between the blood and arterial wall, no-slip conditions are used for the fluid mechanics computations. The hemodynamic force at the interface is applied as external force in the structural mechanics computations. We note that the difference of the hemodynamic force from the level at the beginning of cardiac cycle is used in the simulations. Hence P_0 and R in Eq. (5) are set to −899.25 Pa and 5.45×10^9 Pa s/m^3. The boundary displacements at the inlet and two outlets of the artery are set to zero.

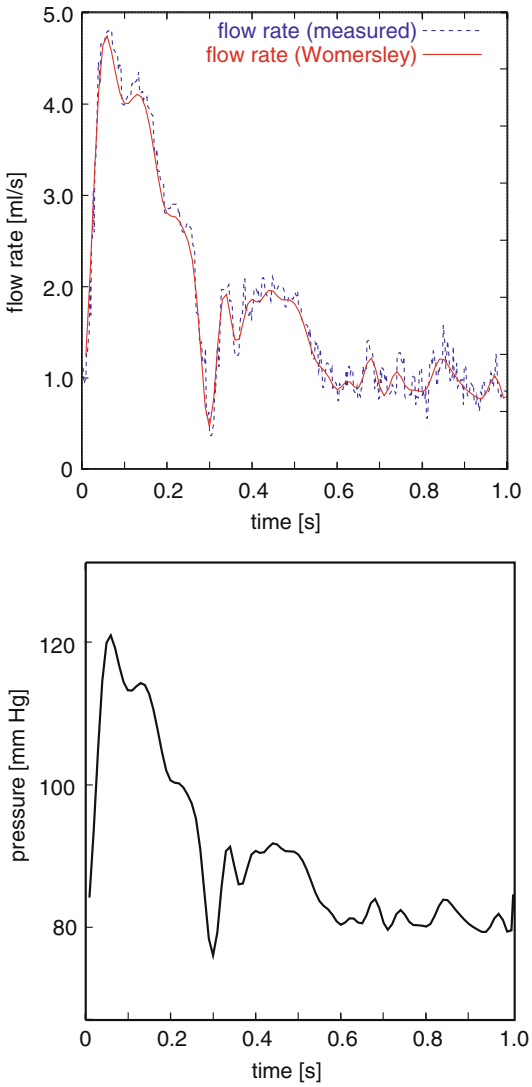

Fig. 2 Flow rate (*top*) and pressure (*bottom*) waveforms at the inlet and outlet. The inflow waveform is shown with the flow waveform calculated based on the velocity recording from ultrasound Doppler velocimeter at the carotid artery of a healthy male volunteer

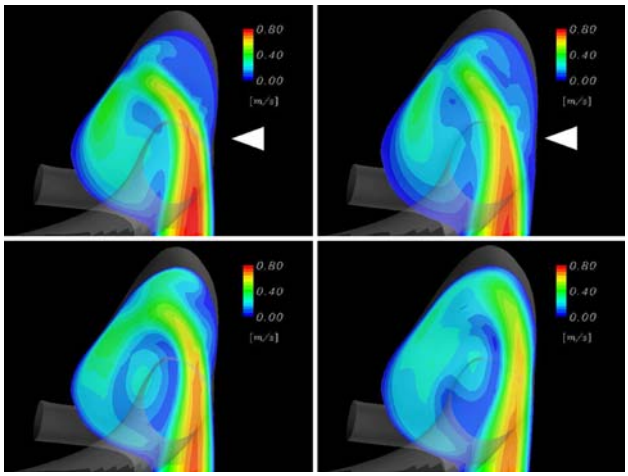

Fig. 3 Flow velocity profiles at the peak systole (*top*) and 0.04 s after the peak (*bottom*). The flows for the rigid arterial wall model are shown on the *left* and those for the LEFS model are shown on the *right*

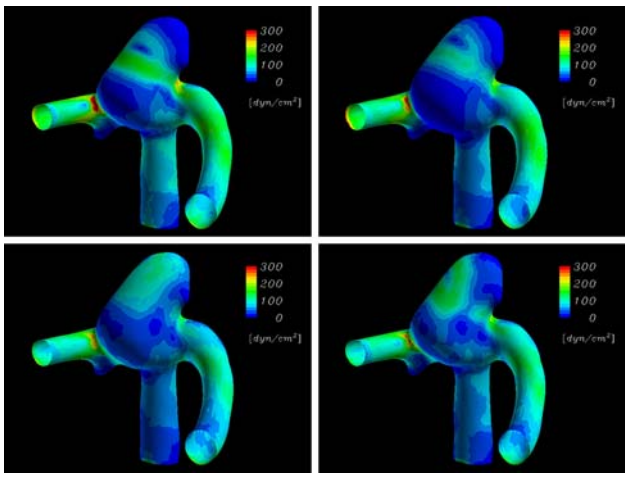

Fig. 4 WSS profiles at the peak systole (*top*) and 0.04 s after the peak (*bottom*). The stresses for the rigid arterial wall model are shown on the *left* and those for the LEFS model are shown on the *right*

3 Results and discussion

3.1 Flow–wall interaction

The shape of an aneurysm was statistically correlated to its rupture risk by Ujiie and co-workers [54]. They reported that a ruptured aneurysm tends to have high aspect ratio (>1.6), defined as the ratio of the depth of an aneurysm to the diameter of the neck. They explained the correlation by a secondary vortex at low velocity near the apex of an aneurysm, i.e. a nearly stagnant vortex occurring near the apex results in very low WSS that degrades the aneurysm wall. The aneurysm in this study has high aspect ratio, 2.81, and is in the range of "risky" aneurysm from that statistical point of view. In an FSI simulation previously carried out [55] with a linearly elastic (LEFS) wall model, a secondary vortex near the apex was observed at the peak systole as shown in Fig. 3, which was expected from the study in [54], whilst the secondary vortex disappeared after the peak systole. On the contrary, the secondary vortex did not disappear when the arterial wall was modeled as a rigid wall (cf. Fig. 3). Figure 4 shows the instantaneous WSS profiles corresponding to the velocity profiles in Fig. 3. The WSS near the apex is much smaller for the rigid arterial wall than it is for the compliant wall, resulting from the secondary vortex at low flow velocity. The differences in the flow patterns are due to the displacement of the arterial wall, indicated by the triangular marker in Fig. 3. In the original aneurysm shape, the wall is curved and bends the flow, making it impinge on the wall across the aneurysm. The flow forms twin vortices after the impingement. The twin-vortex

flow pattern persists after the peak systole when the artery is modeled as a rigid wall, whereas the flow proceeds straight along the wall towards the apex when the wall is compliant. The secondary vortex consequently diminishes. Therefore, particularly in this aneurysm, the interaction between the arterial wall and blood flow plays a significant role in determining the WSS distribution. Hence this model is used for examining the influence of the arterial constitutive model on FSI analysis of aneurysms.

3.2 Dependence of the wall deformation on the structural model

Figures 5, 6 and 7 show the displacement of the lumenal-side arterial wall for the three wall constitutive models. The displacement patterns are similar for all three cases. There are local maxima of displacement on both sides of the aneurysm around the neck of the aneurysm, particularly at the peak systole. The maximum displacement at the peak systole is 0.333, 0.346 and 0.222 mm for LESS, LEFS and HE models, respectively. The local maximum displacement on the inferior side is larger than those on the superior side for all the cases. By comparing Figs. 5 and 6, we see that the displacement for the LESS model is generally smaller than it is for the LEFS model, i.e. the influence of small-strain assumption appears as slight stiffening. This trend is inherent from a theoretical

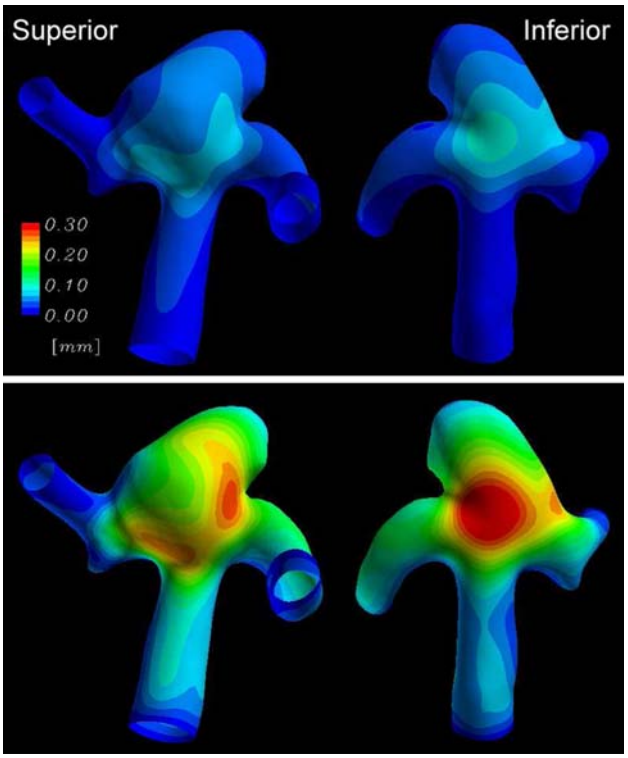

Fig. 6 Displacement profiles for the LEFS model at the beginning of the cardiac cycle (*top*) and the peak systole (*bottom*)

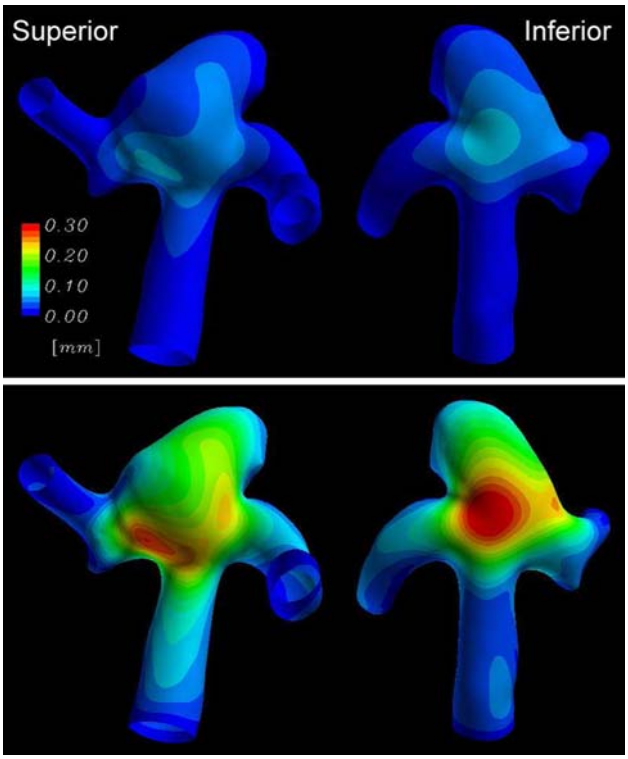

Fig. 5 Displacement profiles for the LESS model at the beginning of the cardiac cycle (*top*) and the peak systole (*bottom*)

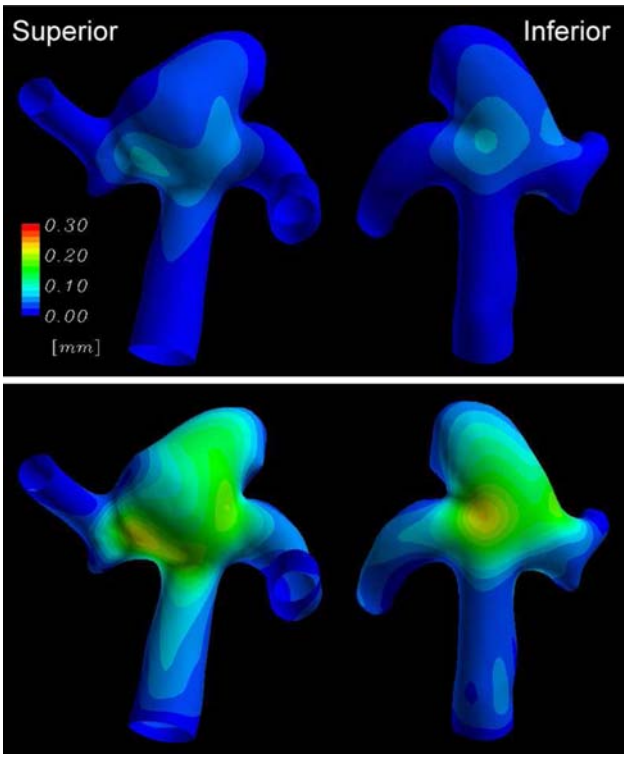

Fig. 7 Displacement profiles for the HE model at the beginning of the cardiac cycle (*top*) and the peak systole (*bottom*)

solid mechanics point of view; the change in the wall thickness is taken into account in evaluating the stresses when finite strain is employed, and an aneurysm wall thinner after inflation is less resistant to inner pressure than the original aneurysmal wall is, which is the reference geometry for evaluating the stresses with the LESS model. The displacement is much smaller for the HE model than that for the linearly elastic models although the displacement patterns are similar to what we get with the other two models. The maximum displacement for the HE model is approximately 64% of that for the LEFS model. We note that the difference in the maximum displacement between the superior and inferior sides for the HE model is smaller than that for the linearly elastic models. The maximum displacement on the superior side is 0.281, 0.274 and 0.219 mm for the LESS, LEFS and HE models. This is because the HE model tends to be stiffer under large strains, i.e. drastic local peaks are not likely to occur with the HE model and the peaks of the displacement patterns become more uniform.

The displacement patterns indeed depend on the material properties and the way the experimental results are reflected including the effect of the residual stresses. Determining the material properties and reflecting the influence of the residual stresses are also widely discussed topics [47,56,57]. We plan to consider this point in our future in this studies.

3.3 Dependence of the FSI on the structural model

The influence of the wall model on the FSI is the primary interest in this study. Figure 8 shows the velocity profile for the LESS and HE models at the peak systole and 0.04 s after the peak, the same time points as those in Fig. 3. For both cases, at the peak systole the flow from the inlet entering the aneurysm along the inferior side of the wall is bent toward the other side and impinges on the wall similar to what we had for the rigid-wall and LEFS models (cf. Fig. 3). The flow is split and forms two vortices in the cross-section: a large vortex in the lower part of the aneurysm and a nearly stagnant vortex near the apex. At 0.04 s after the peak, however, for both models the main stream entering the aneurysm flows along the inferior side wall to the apex. This is because of the deformation of the wall in the middle of the aneurysm on the inferior side, as discussed in Sect. 3.1. The secondary vortex observed at the peak systole disappears for the LESS, LEFS (cf. Fig. 3) and HE models, although for HE model there is a small flow separation region near the apex on the inferior side. Therefore it is clear that the flow patterns in the aneurysm and their time evolution are similar for all compliant wall cases.

A consequence of the above-mentioned time evolution of the flow patterns in the aneurysm is observed in the WSS profiles shown in Fig. 9. At the peak systole, the band-like region of relatively high WSS ($\sim$150 dyn/cm^2) is observed similar

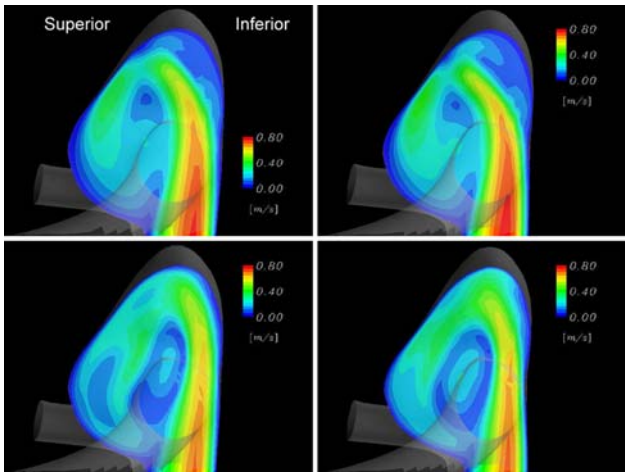

Fig. 8 Flow velocity profiles at the peak systole (*top*) and 0.04 s after the peak (*bottom*) for the LESS (*left*) and HE (*right*) models

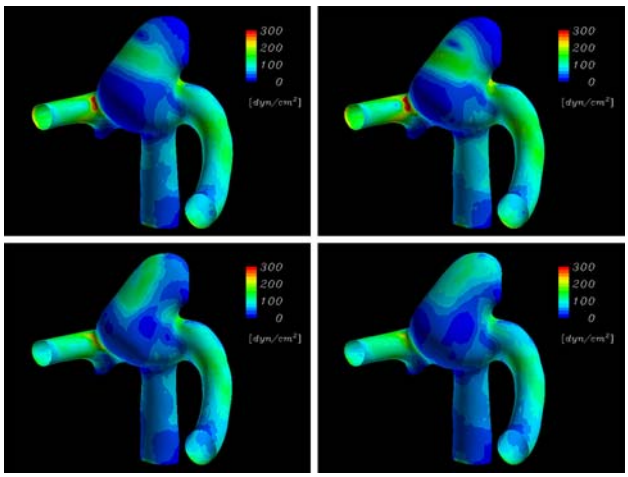

Fig. 9 WSS profiles at the peak systole (*top*) and 0.04 s after the peak (*bottom*) for the LESS (*left*) and HE (*right*) models

to the two cases (rigid-wall and LEFS) previously shown. After the peak systole, the region of high WSS spreads on the aneurysm wall toward the apex. Knowing the behavior of the low WSS near the apex is an important factor in investigating the rupture risk of the aneurysm according to epidemiological and biological studies; degradation of the aneurysm wall tissue due to the low WSS region explains well the statistical correlation of the aneurysm shape to the rupture of aneurysm [54]. Biological evidences indicating a relationship between the WSS and pathological state of the arterial wall [1,58] also back up the explanation.

Figure 10 shows the WSS profile near the apex. To focus on the area of low WSS, the color range is limited to 0 to 50 dyn/cm^2. The minimum WSS in the vicinity of the apex (at the point indicated by a circle in the figure) is 9.29 dyn/cm^2 for the rigid-wall model, which is significantly lower compared to the other parts such as the arterial wall downstream

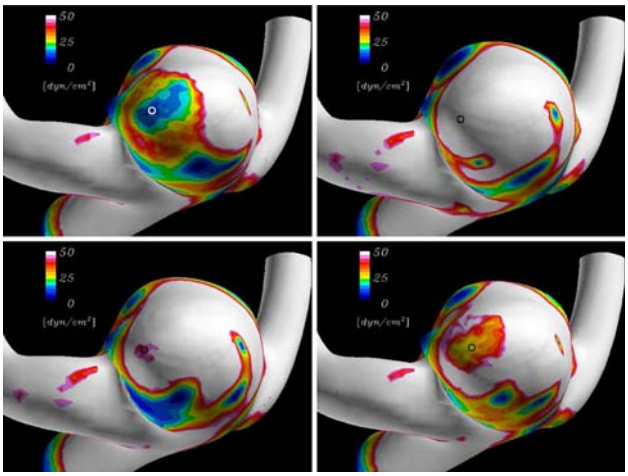

Fig. 10 WSS profiles near the apex of the aneurysm at 0.04 s after the peak systole. *Top left* rigid wall, *top right* LESS model, *bottom left* LEFS model, *bottom right* HE model

of the bifurcation (>50 dyn/cm^2). The minimum WSS in the vicinity of the apex is 54.4 dyn/cm^2 for the LESS model, 41.9 dyn/cm^2 for the LEFS model and 22.9 dyn/cm^2 for the HE model, all higher than the level in the rigid-wall case. Because of the small flow separation region, the flow near the apex is slightly slower for the HE model and the WSS is consequently lower than it is in the other two compliant-wall cases. However, the minimum WSS near the apex is still higher than that for the rigid-wall case. The influence of the material model does not alter the FSI pattern in an aneurysm although the magnitude of the WSS near the apex is affected. In an earlier study [55], we hypothesized that the reason that the aneurysm of this subject remains unruptured despite the high aspect ratio is the disappearance of the stagnant flow region near the apex of the aneurysm, and the aneurysmal wall is consequently exposed to relatively high WSS due to the FSI. The explanation makes sense independent of the wall model, as long as the aneurysm wall is compliant.

The results show that differences in the wall models do not significantly alter the flow–wall interaction analysis of an aneurysm. The results would be more accurate if we employ a method for determining the material properties in a way that represents the subject-specific information. Although the aneurysm wall thickness is assumed to be uniform 300 μm in this study, the wall thickness for ruptured human intracranial saccular aneurysms is very small, approximately 50 μm [59]. A hyper-elastic constitutive model is the most promising approach for FSI computations with such a thin-wall structure, especially in the grown-up stage of an aneurysm. However, the results show that the linearly elastic wall model is still useful for qualitative investigation of the aneurysm FSI, particularly in the early stages of the aneurysm where the wall thickness is expected to be comparable to the arterial wall thickness.

4 Conclusions

FSI simulations employing three different wall models of cerebral aneurysms were carried out: linearly elastic material with small-strain assumption, linearly elastic material with finite strain, and hyper-elastic constitutive model. The displacement profiles and FSI patterns were compared to investigate the impact of the differences in the wall models in patient-specific FSI computations. The displacement profiles were similar for all models, although the maximum displacement for the hyper-elastic model is 36% smaller than that for the linearly elastic material model with finite strain. The differences in the deformation behavior do not alter the flow patterns in the aneurysm. The minimum WSS near the apex is 36% smaller for the hyper-elastic model than that for the linearly elastic models, but a stagnant secondary-vortex generated at the peak systole near the apex of the aneurysm disappears in all cases with a compliant arterial wall, independent of the arterial constitutive model. The results indicate that the linearly elastic models can be useful in investigating the aneurysm FSI, although the hyper-elastic model is theoretically more preferred. In our future studies, the hyper-elastic model will be tested further in conjunction with more realistic aneurysm wall thickness.

Acknowledgments The authors thank Dr. Motoharu Hayakawa (Fujita Health University, Japan) and Toshiba Medical, Inc. for providing the CT images and image processing software ALATOVIEW. The authors are also grateful to Professor Motoaki Sugawara (Tokyo Women's Medical University, Japan) for his help in acquiring the velocity waveform. Part of this research was carried out within the framework of the project "Frontier Simulation Software for Industrial Science (FSIS)" and "Revolutionary Simulation Software (RSS)", supported by the IT program of the Ministry of Education, Culture, Sports, Science and Technology (MEXT). The last author was supported in part by a Seed Grant from the Gulf Coast Center for Computational Cancer Research funded by John & Ann Doerr Fund for Computational Biomedicine.

References

1. Steiger HJ (1990) Pathophysiology of development and rupture of cerebral aneurysms. Acta Neurochir Suppl 48:1–57
2. Torii R, Oshima M, Kobayashi T, Takagi K, Tezduyar TE (2006) Fluid–structure interaction modeling of aneurysmal conditions with high and normal blood pressures. Comput Mech 38:482–490
3. Komatsu Y, Yasuda S, Shibata T, Ono Y, Hyodo A, Nose T (1994) Management for subarachnoid hemorrhage with negative initial angiography. Neurol Surg (in Japanese) 22:43–49
4. Taylor CL, Yuan Z, Selman WR, Ratcheson RA, Rimm AA (1995) Cerebral arterial aneurysm formation and rupture in 20,767 elderly patients: hypertension and other risk factors. J Neurosurg 83:812–819
5. Torii R, Oshima M, Kobayashi T, Takagi K, Tezduyar TE (2007) Fluid–structure interaction modeling of blood flow and cerebral aneurysm: significance of arterial and aneurysm shape. In: Proceedings of USNCCM9, San Francisco, July

6. Fung YC (1993) Biomechanics: mechanicsl properties of living tissue, 2 edn. Springer, New York
7. Humphrey JD (2002) Cardiovascular solid mechanics. Cells, tissues, and organs. Springer, New York
8. Torii R, Oshima M, Kobayashi T, Takagi K, Tezduyar TE (2007) Influence of wall elasticity in patient-specific hemodynamic simulations. Comput Fluids 36:160–168
9. Baek S, Gleason RL, Rajagopal KR, Humphrey JD (2007) Theory of small on large: Potential utility in computations of fluid–solid interactions in arteries. Comput Methods Appl Mech Eng 196:2070–3078
10. Figueroa CA, Vignon-Clementel IE, Jansen KE, Hughes TJR, Taylor CA (2006) A coupled momentum method for modeling blood flow in three-dimensional deformable arteries. Comput Meth Appl Mech Eng 195:5685–5706
11. Raghavan ML, Vorp DA (2000) Toward a biomechanical tool to evaluate rupture potential of abdominal aortic aneurysm: identification of a finite strain constitutive model and evaluation of its applicability. J Biomech 33(4):475–482
12. DI Martino ES, Vorp D (2003) Effect of variation in intraluminal thrombus constitutive properties on abdominal aortic aneurysm wall stress. Ann Biomed Eng 31:804–809
13. Leung JH, Wright AR, Cheshire N, Crane J, Thom SA, Hughes AD, Xu Y (2006) Fluid structure interaction of patient specific abdominal aortic aneurysms: a comparison with solid stress models. Biomed Eng 5 (online)
14. Bazilevs Y, Calo VM, Zhang Y, Hughes TJR (2006) Isogeometric fluid–structure interaction analysis with applications to arterial blood flow. Comput Mech 38:310–322
15. Tezduyar TE, Sathe S, Cragin T, Nanna B, Conklin BS, Pausewang J, Schwaab M (2007) Modeling of fluid–structure interactions with the space–time finite elements: Arterial fluid mechanics. Int J Numer Meth Fluids 54:901–922
16. Tezduyar TE, Sathe S, Schwaab M, Conklin BS (2008) Arterial fluid mechanics modeling with the stabilized space–time fluid–structure interaction technique. Int J Numer Meth Fluids 57:601–629. doi:10.1002/fld.1633
17. Holzapfel GA, Gasser TC (2000) A new constitutive framework for arterial wall mechanics and a comparative study of material models. J Elast 61:1–48
18. Humphrey JD, Na S (2002) Elastodynamics and arterial wall stress. Ann Biomed Eng 30:509–523
19. Gasser TC, Holzapfel GA (2007) Finite element modeling of balloon angioplasty by considering overstretch of remnant non-diseased tissues in lesions. Comput Mech 40:47–60
20. Hariton I, deBotton G, Gasser TC, Holzapfel GA (2005) How to incorporate collagen fibers orientations in an arterial bifurcation? In: Proceedings of 3rd IASTED international conference on biomechanics, Benidorm, Spain, September
21. Williamson SD, Lam Y, Younis HF, Huang H, Patel S, Kaazempur-Mofrad MR, Kamm RD (2003) On the sensitivity of wall stresses in diseased arteries to variable material properties. J Biomech Eng 125:147–155
22. Karino T, Takeuchi S, Kobayashi N, Motomiya M, Mabuchi S (1993) Fluid dynamics of cerebrovascular disease (in Japanese). Neurosurgeons 12:15–24
23. Tezduyar TE (1992) Stabilized finite element formulations for incompressible flow computations. Adv Appl Mech 28:1–44
24. Tezduyar TE, Behr M, Liou J (1992) A new strategy for finite element computations involving moving boundaries and interfaces – the deforming-spatial-domain/space–time procedure: I. The concept and the preliminary numerical tests. Comput Methods Appl Mech Eng 94(3):339–351
25. Tezduyar TE, Behr M, Mittal S, Liou J (1992) A new strategy for finite element computations involving moving boundaries and interfaces—the deforming-spatial-domain/space–time procedure: II. Computation of free-surface flows, two-liquid flows, and flows with drifting cylinders. Comput Methods Appl Mech Eng 94(3):353–371
26. Tezduyar TE (2003) Computation of moving boundaries and interfaces and stabilization parameters. Int J Numer Methods Fluids 43:555–575
27. Hughes TJR, Brooks AN (1979) A multi-dimensional upwind scheme with no crosswind diffusion. In: Hughes TJR (ed) Finite element methods for convection dominated flows, AMD, vol 34, ASME, New York, pp 19–35
28. Brooks AN, Hughes TJR (1982) Streamline upwind/Petrov-Galerkin formulations for convection dominated flows with particular emphasis on the incompressible Navier–Stokes equations. Comput Methods Appl Mech Eng 32:199–259
29. Tezduyar TE, Mittal S, Ray SE, Shih R (1992) Incompressible flow computations with stabilized bilinear and linear equal-order-interpolation velocity-pressure elements. Comput Methods Appl Mech Eng 95:221–242
30. Hughes TJR, Franca LP, Balestra M (1986) A new finite element formulation for computational fluid dynamics: V. Circumventing the Babuška–Brezzi condition: a stable Petrov–Galerkin formulation of the Stokes problem accommodating equal-order interpolations. Comput Methods Appl Mech Eng 59:85–99
31. Tezduyar T, Aliabadi S, Behr M, Johnson A, Mittal S (1993) Parallel finite-element computation of 3D flows. Computer 26(10):27–36
32. Tezduyar TE, Aliabadi SK, Behr M, Mittal S (1994) Massively parallel finite element simulation of compressible and incompressible flows. Comput Methods Appl Mech Eng 119:157–177
33. Tezduyar T, Aliabadi S, Behr M, Johnson A, Kalro V, Litke M (1996) Flow simulation and high performance computing. Comput Mech 18:397–412
34. Tezduyar TE (1999) CFD methods for three-dimensional computation of complex flow problems. J Wind Eng Ind Aerodyn 81:97–116
35. Tezduyar TE (2001) Finite element methods for flow problems with moving boundaries and interfaces. Arch Comput Methods Eng 8:83–130
36. Tezduyar TE (2006) Interface-tracking and interface-capturing techniques for finite element computation of moving boundaries and interfaces. Comput Methods Appl Mech Eng 195:2983–3000
37. Tezduyar TE (2007) Finite elements in fluids: stabilized formulations and moving boundaries and interfaces. Comput Fluids 36:191–206
38. Tezduyar TE (2007) Finite elements in fluids: special methods and enhanced solution techniques. Comput Fluids 36:207–223
39. Mittal S, Tezduyar TE (1995) Parallel finite element simulation of 3D incompressible flows—fluid–structure interactions. Int J Numer Methods Fluids 21:933–953
40. Kalro V, Tezduyar TE (2000) A parallel 3D computational method for fluid–structure interactions in parachute systems. Comput Methods Appl Mech Eng 190:321–332
41. Tezduyar T, Osawa Y (2001) Fluid–structure interactions of a parachute crossing the far wake of an aircraft. Comput Methods Appl Mech Eng 191:717–726
42. Stein KR, Benney RJ, Tezduyar TE, Leonard JW, Accorsi ML (2001) Fluid–structure interactions of a round parachute: modeling and simulation techniques. J Aircraft 38:800–808
43. Tezduyar TE, Sathe S, Keedy R, Stein K (2006) Space–time finite element techniques for computation of fluid–structure interactions. Comput Methods Appl Mech Eng 195:2002–2027
44. Tezduyar TE, Sathe S, Stein K (2006) Solution techniques for the fully-discretized equations in computation of fluid–structure interactions with the space–time formulations. Comput Methods Appl Mech Eng 195:5743–5753

45. Tezduyar TE, Sathe S (2007) Modeling of fluid–structure interactions with the space–time finite elements: solution techniques. Int J Numer Methods Fluids 54:855–900
46. Hisada T, Noguchi H (1995) Fundamentals and applications of nonlinear finite element method (in Japanese). Maruzen, Tokyo
47. Delfino A, Stergiopulos N, Moore JEJr, Meister JJ (1997) Residual strain effects on the stress field in a thick wall finite element model of the human carotid bifurcation. J Biomech 30:777–786
48. Tezduyar TE (2004) Finite element methods for fluid dynamics with moving boundaries and interfaces. In: Stein E, De Borst R, Hughes TJR (eds) Encyclopedia of computational mechanics, vol 3, Fluids, Chap 17, Wiley, New York
49. Tezduyar TE, Behr M, Mittal S, Johnson AA (1992) Computation of unsteady incompressible flows with the finite element methods—space–time formulations, iterative strategies and massively parallel implementations. In: New methods in transient analysis, PVP-vol 246/AMD-vol 143, ASME, New York, pp 7–24
50. Torii R, Oshima M, Kobayashi T, Takagi K, Tezduyar TE (2006) Computer modeling of cardiovascular fluid–structure interactions with the deforming-spatial-domain/stabilized space–time formulation. Comput Methods Appl Mech Eng 195:1885–1895
51. McDonald DA (1974) Blood flow in arteries, 2nd edn. Edward Arnold, London
52. Hayashi K, Handa H, Nagasawa S, Okumura A, Moritake K (1980) Stiffness and elastic behavior of human intracranial and extracranial arteries. J Biomech 13:175–184
53. Womersley JR (1955) Method for the calculation of velocity, rate of flow and viscos drag in arteries when the pressure gradient is known. J Physiol 127:553–563
54. Ujiie H, Tamano Y, Sasaki K, Hori T (2001) Is the aspect ratio a reliable index for predicting the rupture of a saccular aneurysm. Neurosurgery 48(3):495–503
55. Torii R, Oshima M, Kobayashi T, Takagi K, Tezduyar TE (2007) Numerical investigation of the effect of hypertensive blood pressure on cerebral aneurysm—dependence of the effect on the aneurysm shape. Int J Numer Methods Fluids 54:995–1009
56. Holzapfel GA (2003) Biomechanics of Soft Tissue in Cardiovascular Systems, chapter Structural and numerical models for the (visco)elastic response of arterial walls with residual stresses. Number 141 in CISM courses and lectures. Springer, New York
57. Raghavan ML, Trivedi S, Nagaraj A, McPherson DD, Chandran KB (2004) Three-dimensional finite element analysis of residual stress in arteries. Ann Biomed Eng 32:257–263
58. Malek AM, Alper SL, Izumo S (1999) Hemodynamic shear stress and its role in atherosclerosis. J Am Med Assoc 282:2035–2042
59. Abruzzo T, Shengelaia GG, Dawson RCIII, Owens DS, Cawley CM, Gravanis MB (1998) Histologic and morphologic comparison of experimental aneurysms with human intracranial aneurysm. Am J Neuroradiol 19:1309–1314